

Nanoparticle-mediated targeting of phosphatidylinositol-3-kinase signaling inhibits angiogenesis

Rania Harfouche · Sudipta Basu · Shivani Soni ·
Dirk M. Hentschel · Raghunath A. Mashelkar ·
Shiladitya Sengupta

Received: 16 February 2009 / Accepted: 22 July 2009 / Published online: 14 August 2009
© Springer Science+Business Media B.V. 2009

Abstract

Objective Dysregulation of the phosphatidylinositol-3-kinase (PI3K) signaling pathway is a hallmark of human cancer, occurring in a majority of tumors. Activation of this pathway is critical for transformation and also for the angiogenic switch, which is a key step for tumor progression. The objective of this study was to engineer a PI3K inhibitor-loaded biodegradable nanoparticle and to evaluate its efficacy.

Methods and results Here we report that a nanoparticle-enabled targeting of the PI3K pathway results in inhibition of downstream Akt phosphorylation, leading to inhibition of proliferation and induction of apoptosis of B16/F10 melanoma. It, however, failed to exert a similar activity on MDA-MB-231 breast cancer cells, resulting from reduced internalization and processing of nanoparticles in this cell

line. Excitingly, the nanoparticle-enabled targeting of the PI3K pathway resulted in inhibition of endothelial cell proliferation and tubulogenesis, two key steps in tumor angiogenesis. Furthermore, it inhibited both B16/F10- and MDA-MB-231-induced angiogenesis in a zebrafish tumor xenotransplant model.

Conclusion Our study, for the first time, shows that targeting of the PI3K pathway using nanoparticles can offer an attractive strategy for inhibiting tumor angiogenesis.

Keywords Angiogenesis · Nanoparticles · PI3 kinase

Rania Harfouche and Sudipta Basu have contributed equally to this work.

Electronic supplementary material The online version of this article (doi:[10.1007/s10456-009-9154-4](https://doi.org/10.1007/s10456-009-9154-4)) contains supplementary material, which is available to authorized users.

R. Harfouche · S. Basu · S. Soni · R. A. Mashelkar ·
S. Sengupta
Harvard-MIT Division of Health Sciences and Technology,
Brigham and Women's Hospital, Harvard Medical School,
Boston, MA 02115, USA

R. Harfouche · S. Basu · S. Soni · D. M. Hentschel ·
S. Sengupta
Department of Medicine, Brigham and Women's Hospital,
Harvard Medical School, Boston, MA 02115, USA

S. Sengupta (✉)
Harvard Medical School, Brigham and Women's Hospital,
Room 317, 65 Landsdowne street, Cambridge, MA 02139, USA
e-mail: shiladit@mit.edu

One of the best characterized oncogenic signal transduction cascades is the phosphatidylinositol-3-kinase (PI3K)-Akt pathway, which is dysregulated in a majority of tumors [1]. PI3K is generally recruited downstream of activated receptor tyrosine kinases, G-protein-coupled receptors or integrins at the plasma membrane, where it catalyzes the addition of a phosphate group at the 3'-position of the inositol ring of phosphoinositide/phosphatidylinositol (PI), which binds to the pleckstrin-homology domain of multiple proteins [2]. Activating mutations of the gene that encodes the catalytic subunit of class 1A PI3K have been implicated in ovarian and lung tumors [3, 4]. Similarly, phosphatase PTEN, which deactivates PI3K, has been shown to be mutationally or post translationally inactivated or inhibited in other tumors, such as in glioblastoma, breast, melanoma, lung, and hepatocellular carcinomas [5–9]. Furthermore, PI3K signaling has been implicated in tumor angiogenesis downstream of growth factors such as vascular endothelial growth factor and hepatocyte growth factor [10, 11]. Thus, inhibition of PI3K holds the promise of a multipronged

strategy for tumor inhibition. However, clinical use of PI3K inhibitors has faced hurdles arising from potential systemic toxicities.

Nanotechnology holds great promise for the diagnosis and treatment of cancer [12, 13]. Nanovector-based therapeutics have been preferentially delivered into tumors as opposed to other tissue by exploiting the enhanced permeability and retention (EPR) effect [12], a property that permits nanoscale structures to be taken up passively into tumors. Traditionally, nanovectors have been used to deliver cytotoxic agents that are either difficult to formulate as a result of hydrophobicity, such as in the case of paclitaxel [14], or exhibit systemic toxicity, such as cardiotoxicity as seen with doxorubicin [15]. Recently, we demonstrated that a nanotechnology-based targeting of the mitogen-activated protein kinase pathway predisposes the tumor to the effects of cytotoxic chemotherapeutic agents, indicating that combining signal transduction inhibitors with nanotechnology can emerge as a new paradigm for cancer therapy [16]. In the current study, we engineered a biodegradable polymeric nanoparticle as a vehicle for LY294002 to target the PI3K oncogenic signaling pathway. LY294002 [2-(4-morpholinyl)-8-phenylchromone] selectively inhibits PI3K by competitively binding the ATP-binding pocket of PI3K's catalytic domain ($IC_{50} = 1.40 \mu\text{M}$) [17], and is hydrophobic, making it a suitable drug for formulation within a nanoparticle. We demonstrate that a nanoparticle-mediated delivery of a signal transduction inhibitor of PI3K can block angiogenesis in vitro and in vivo.

Materials and methods

Materials

All the solvents were purchased from Sigma–Aldrich (St. Louis, MO) and Fisher (Pittsburgh, PA), unless otherwise stated and used without any further purification. The poly (lactic-*co*-glycolic acid) (MW ~66 kDa) having a lactic/glycolic molar ratio of 50/50 was procured from Lakeshore biomaterials (Brookwood Pharmaceutical Inc., AL). LY294002 was purchased from Tocris Bioscience (Ellisville, MO). Epon-812 resin was purchased from Electron Microscopy Sciences (Hatfield, PA). Polyvinyl alcohol (PVA) was purchased from Sigma–Aldrich. *CellTiter 96 AQueous One Solution Cell Proliferation (MTS) Assay* kit was obtained from Promega Corporation (Madison, WI). AnnexinV-Alexa Fluor 488, the LysoTracker Red probe and the QTracker Red cell labeling kit were all from Invitrogen (Carlsbad, CA). Monoclonal antibody specific for actin was purchased from Sigma–Aldrich, whereas polyclonal antibodies against the phosphorylated (p-AKT) and total form (AKT) of AKT were from Cell Signaling

Technology (Danvers, MA). Vascular endothelial cell growth factor (VEGF) was from R&D Systems (Minneapolis, MN). Matrigel basement membrane matrix was obtained from BD Biosciences (San Jose, CA).

Synthesis of LY294002-encapsulated nanoparticle (NP-LY)

Nanoparticles (NP) were formulated using an emulsion-solvent evaporation technique. Briefly, 50 mg PLGA was dissolved in 2.5 ml acetone and mixed with 3 mg of LY294002 (dissolved in 0.5 ml methanol). The entire solution was emulsified into 25 ml of 2% aqueous solution of PVA (80% hydrolyzed, Mw ~9,000–10,000) by slow injection with constant homogenization using a tissue homogenizer (Fisher Scientific Tissuemiser Homogenizer, probe dimension: L x Dia. x Overall L = 8.3 x 0.7 x 28.6 cm). The emulsion was added to a 100 ml 0.2% aqueous solution of PVA (80% hydrolyzed, Mw ~9,000–10,000) with rapid stirring for 4 h at room temperature to evaporate any residual acetone and methanol. The desired NP size fraction was recovered by ultracentrifugation at 20,000 and 80,000× g and the NPs were lyophilized for 24 h. Sizing was performed by dynamic light scattering (DLS) using a Malvern Nanotetasizer and transmission electron microscopy (TEM) using a Philips system. To quantify the LY294002 loading in the NPs, 5 mg of lyophilized NP-LY was completely dissolved in 500 μl DMF (the polymeric nanoparticles were completely dissolved in DMF, which ensures the complete release of all LY29400 from the NP). The absorbance of LY294002 was measured by UV–VIS spectra at 298 nm wavelength, at which PLGA shows no absorbance. Furthermore, addition of the same concentration of empty PLGA NP to a solution of LY294002 in DMF showed that PLGA does not interfere with UV–VIS spectra of LY294002. The loading was quantified against a standard absorbance–concentration linear plot, and expressed as the amount of LY294002 per mg of NP-LY was quantified.

Transmission electron microscopy (TEM) of the nanoparticles

The NP were fixed in 2.5% gluteraldehyde, 3% paraformaldehyde with 5% sucrose in 0.1 M sodium cacodylate buffer (pH = 7.4), embedded in low temperature agarose and post fixed in 1% OsO₄ in veronal-acetate buffer. The sample was stained in a block overnight with 0.5% uranyl acetate in veronal-acetate buffer (pH = 6.0) then dehydrated and embedded in epon-812 resin. Sections were cut on a Leica ultra cut UCT at a thickness of 70 nm using a diamond knife, stained with 2.0% uranyl acetate followed by 0.1% lead citrate and examined using a Philips EM410.

Physicochemical release kinetics characterization

LY294002-encapsulated NP were suspended in 500 μ l of different cell lysates (MDA-MB-231, B16-F10, and HUVEC in buffer) and sealed in a dialysis bag (MWCO \sim 1,000 Da). The dialysis bag was incubated in 1 ml of PBS buffer at room temperature with gentle shaking. An aliquot (10 μ l) was extracted from the incubation medium at predetermined time intervals, dissolved in 90 μ l DMF, and released LY294002 was quantified by UV–VIS spectroscopy at characteristic wavelength of LY294002, $\lambda = 298$ nm using absorbance–concentration calibration curve. After withdrawing each aliquot, the incubation medium was replenished by 10 μ l of fresh PBS to keep the outside volume constant.

Cell culture

Cancer cells were obtained from American Type Tissue Culture Collection (Rockville, MD) and were maintained in DMEM supplemented with 10% FBS and antibiotic/antimycotic (all from Invitrogen). MDA-MB-231 human breast adenocarcinoma, B16-F10 mouse melanoma and Lewis lung carcinoma cells were grown on 100 mm dishes and subcultured using trypsin (0.25%) and EDTA (0.01%). Cells were switched to 1% serum overnight prior to drug addition to synchronize the cells. All cells were seeded at densities between 2,500 and 5,000 cells/cm².

Human umbilical vein endothelial cells (HUVEC) were obtained from Cambrex Bio Science (Hopkinton, MA) and cultured in EGM-2 medium according to the manufacturer's protocol. Cells were used between passages 2 and 5. The cells were subcultured following trypsin (0.025%) and EDTA (0.01%) application. For all experiments, HUVEC were synchronized overnight using serum reduced medium (0.1% FBS) prior to drug and growth factor addition, except in the case of the tube assay. For the MTS assay and immunoblotting, HUVEC were stimulated with 5 nM of VEGF.

MTS cytotoxicity assay

Cancer or endothelial cells in 96-well plates (seeding density between 2,500 and 5,000 per well) were incubated with various doses of free LY294002 or NP-LY (equivalent dose of free LY294002) for 24, 48, and 72 h. The percentage of viable cells were then quantified with 3-(4,5-Dimethylthiazol-2-yl)-5-(3-carboxymethoxyphenyl)-2-(4-sulfophenyl)-2H-tetrazolium (MTS) from the *CellTiter 96 AQueous One Solution* kit. Briefly, the cells were washed with PBS, incubated with 0.3 mg/ml of MTS, in basal medium without phenol red for 4 h at 37°C and absorbance

was then measured at 490 nm in a plate reader (Versamax, Molecular Devices, Sunnyvale, CA). Final absorbance, corresponding to cell viability, was plotted after subtracting background values from each data point.

AnnexinV-FITC apoptosis study

Cells grown in 6-well plates were treated with drugs for 48 h, and incubated with 5 μ l AnnexinV-Alexa Fluor 488 in binding buffer (10 mM HEPES, 140 mM NaCl, 2.5 mM CaCl₂, pH 7.4) for 15 min in the dark, according to the manufacturer's protocol. Cells were then washed with binding buffer, counterstained with propidium iodide and immediately analyzed using a Becton Dickinson FACSCalibur flow cytometer (excitation 488 and 585 nm, respectively). AnnexinV-Alexa Fluor 488, propidium iodide or both were omitted for the negative controls.

Nanoparticle internalization studies

Two experiments were performed in order to determine the percentage of drug being internalized by the cells. In the first such experiment, we used Lysotracker probes, which accumulate in the acidic compartments of live cells and can hence be used to track drug uptake. MDA-MB-231, B16-F10 and HUVEC cells were seeded on glass coverslips in 24-well plates until subconfluence, and then treated with 5.6 mg/ml FITC-conjugated nanoparticles (FITC-NP) for a time-course ranging from 30 min to 24 h. At the indicated times, cells were washed twice in PBS and incubated in Lysotracker Red (Ex: 577 nm; Em: 590 nm) for 30 min at 37°C. Cells were then washed again, fixed in 4% paraformaldehyde and mounted using Prolong Gold antifade reagent (Invitrogen). Images taken in three random fields were captured at 20 and 40 \times using an inverted microscope (Nikon Eclipse, Melville, NY) equipped with blue and green filters in order to visualize FITC-NP and Lysotracker Red fluorescence, respectively. Cells incubated with either only FITC-NP or Lysotracker Red served as negative controls.

To synthesize FITC-PLGA conjugate, PLGA (50 mg) was dissolved in 750 μ l dichloromethane (DCM). *N*-hydroxy succinimide (10 mg) and *N*-(3-Dimethylaminopropyl)-*N*-ethylcarbodiimide (15 mg) were added into the reaction mixture and stirred at room temperature for 2 h. FITC (6 mg) was dissolved in a mixture of DCM (25 μ l) and pyridine (25 μ l). FITC solution in pyridine was added into the activated PLGA solution and the reaction mixture was stirred at 4°C for 24 h in dark. The reaction was diluted with 50 ml DCM and quenched with 0.1 N HCl solution. The organic layer was extracted with DCM

(20 ml \times 2), washed with water (10 ml \times 2), brine (20 ml) and dried over anhydrous sodium sulfate. The organic layer was filtered and evaporated to obtain the crude product. The PLGA-FITC conjugate was precipitated out from the crude product by addition of diethyl ether (40 ml). The polymer was centrifuged at 3,220 \times g for 30 min. The supernatant was discarded and the polymer was washed thoroughly by diethyl ether (5 ml \times 3) and dried under vacuum overnight. The nanoparticles were engineered from PLGA-FITC conjugate using the protocol described earlier.

In the second experiment, HUVECs were incubated for 6 h (the time-point where maximal drug internalization was observed from the previous assay) with 50 μ M LY or NP-LY, after which time, cells were washed with PBS and collected in basic lysis buffer (pH 7.5) containing 50 mM HEPES, 150 mM NaCl, 100 mM sodium fluoride, 1 mM sodium orthovanadate, 5 mM EDTA, 1 mM PMSF, 2 μ g/ml leupeptin, 5 μ g/ml aprotinin and 0.5% Triton-X-100. The lysed cells were lyophilized to remove water and then suspended in 100 μ l of DMF and shaken for 30 min to dissolve all internalized LY294002 (free and encapsulated). The undissolved lysed cells were centrifuged at 25,000 \times g for 10 min. The supernatant was collected and LY294002 was quantified by UV–VIS spectra at wavelength $\lambda = 298$ using a standard concentration–absorbance

curve. Untreated cells were processed similarly and were used as blanks.

Immunoblotting

Cancer or endothelial cells were washed twice with PBS and directly lysed in 3 \times loading buffer containing 12% sodium dodecyl sulfate, 15% 2-mercaptoethanol, 1 mM sodium orthovanadate and protease inhibitor cocktail tablets from Roche Applied Science (Indianapolis, IN). Cells were further homogenized by passing the lysates three times through an insulin needle. Samples were then heated for 5 min at 100°C and equal amounts loaded onto tris-glycine SDS–polyacrylamide gels. Proteins were electrophoretically transferred onto polyvinylidene difluoride membranes, blocked for 1 h with 7% nonfat dry milk and subsequently incubated overnight at 4°C with primary antibodies directed against the phosphorylated or total forms of Akt. Proteins were detected with horseradish peroxidase-conjugated antirabbit secondary antibodies and Lumi-LightPLUS Western Blotting Substrate (Roche Applied Science). The blots were developed using Gene-Snap and optical densities of the protein bands quantified using GeneTools (both from SynGene, Frederick, MD). Predetermined molecular weight standards were used as markers. Proteins were normalized against actin.

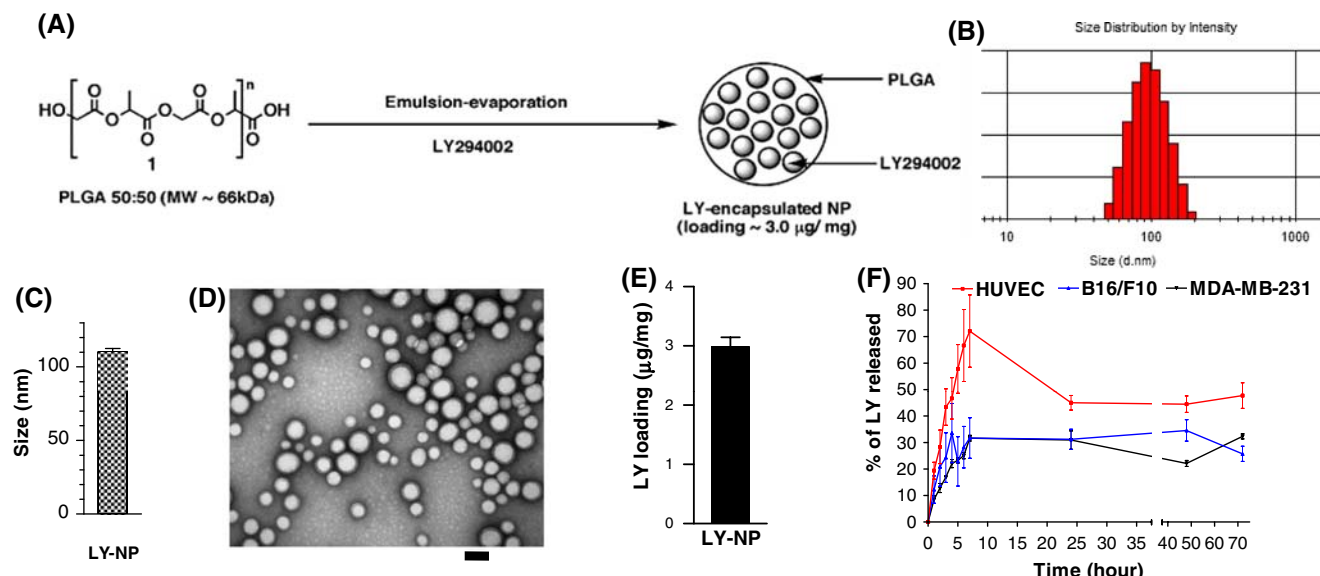


Fig. 1 Synthesis and characterization of LY294002 encapsulated nanoparticle: **a** Schematic representation of the synthesis of LY294002 encapsulated nanoparticles by emulsion–evaporation technique. **b** Size distribution (in nm) of the LY294002 encapsulated nanoparticles by dynamic light scattering (DLS) experiment, and **c** graph showing mean \pm SEM size of the nanoparticles from $n = 6$ independent experiments. **d** Transmission electron microscopy (TEM) image of LY294002 encapsulated nanoparticles. Bar represents

125 nm. **e** Graph shows the mean \pm SEM loading of LY294002 in the nanoparticle matrix ($n = 7$) as quantified using absorbance against a standard absorbance curve. **f** Graph shows release kinetics of LY294002 from the nanoparticle when incubated with different cell lysates. The values on the Y-axis represent the % amount of LY294002 released from the NP-LY (the % amount of LY294002 = amount of LY released \times 100/total amount of LY encapsulated in NP-LY)

HUVEC tube assay

We quantified the effect of free LY294002 or NP-LY using an in vitro angiogenic assay as follows. HUVEC were seeded in 24-well plates at a density of 30,000 per well, on glass coverslips that had been previously coated with 300 μ l matrigel (diluted 1:2 in PBS) for 30 min at 37°C, in medium containing 50 μ M of free LY294002 or nanoparticle containing an equal amount of LY294002, and incubated for 24 or 48 h. At each time point, cells were fixed with 4% paraformaldehyde and immediately visualized under inverted light microscopy at 20 \times magnification (Nikon Eclipse). Ten fields of view per coverslip with five coverslips per conditions were captured, and furthermore three morphometric methods were used (NIS-elements software, Nikon, Melville, NY) to quantify the results. In the first such method, we measured the length of each tube per field, in the second we measured the associated number of nodes, whereas in the third method, we used a standard graticule to measure the number of vessels falling on each intersection.

Zebrafish xenograft assays

In order to assess the effect of NP-LY on in vivo angiogenesis, we used the transparent *Danio Rerio* (zebrafish) model. Zebrafish [TubingenAB] embryos were maintained at 28°C in standard E3 solution buffered with 2 mM HEPES. Forty-eight hour postfertilization (hpf) embryos were anesthetized with 0.04 mg/ml of Tricaine and were dechorionated manually. Embryos were injected in the yolk sac, near the subintestinal vessels, with around 500 cells resuspended in matrigel, in the presence or absence of free LY or NP-LY (equivalent to 200 μ M of LY294002) and with a constant volume of 9.2 nl using a Nanoject II (Drummond Scientific), based on the protocol of Stefania et al. [18]. The embryos were injected with either MDA-MB-231/GFP or B16-F10 cells labeled with the QTracker Red kit, according to the manufacturer's protocol. Images were taken both in real-time and after alkaline phosphatase staining using nitroblue tetrazolium chloride and 5-bromo-4-chloro-3-indolyl phosphate, toluidine salt (Roche, Nutley, NJ), in order to visualize their vasculature. Brightfield and fluorescence imaging of the embryos was performed with a Nikon SMZ1500 stereomicroscope and SPOT Flex camera. Image sequences were obtained with the same set-up and exported as movies to match live flow patterns. The embryos were monitored each day post injection (dpi) in order to generate a cytotoxicity profile of the free drug versus the NP. Morphometric analysis of subintestinal vessels for each fish was done by measuring two independent parameters using the NIS-elements software, resulting in different profiles based on the type of

xenograft. All procedures were approved by Harvard University IACUC.

For the zebrafish assays, MDA-MB-231 cells stably expressing GFP (MDA-MB-231/GFP) were generated using the pAcGFP-C1 expression plasmid (Clontech, Mountain View, CA). This vector contains a codon-optimized GFP gene, which yields maximal expression and prolonged fluorescence in mammalian cells, as well as a gene coding for neomycin resistance, thus allowing for geneticin (G418) selection. 1.5×10^5 MDA-MB-231 cells were seeded in 6-well plates overnight and then transfected with 2 μ g pAcGFP1-C1 using Lipofectin reagent (Invitrogen) for 24 h. Cells were allowed to recover for 24 h, after which time, fresh growth medium supplemented with 1 mg/ml geneticin was added until drug-resistant colonies appeared. These drug resistant cells were then propagated and sorted based on the top 5% of fluorescence using a MoFlo3 cell sorter.

Statistical analysis

All results were expressed as mean \pm SEM of at least triplicate samples. Statistical comparisons were obtained using one-way analysis of variance followed by Newman Keuls Post Hoc test. $P < 0.05$ was considered significant.

Results and discussion

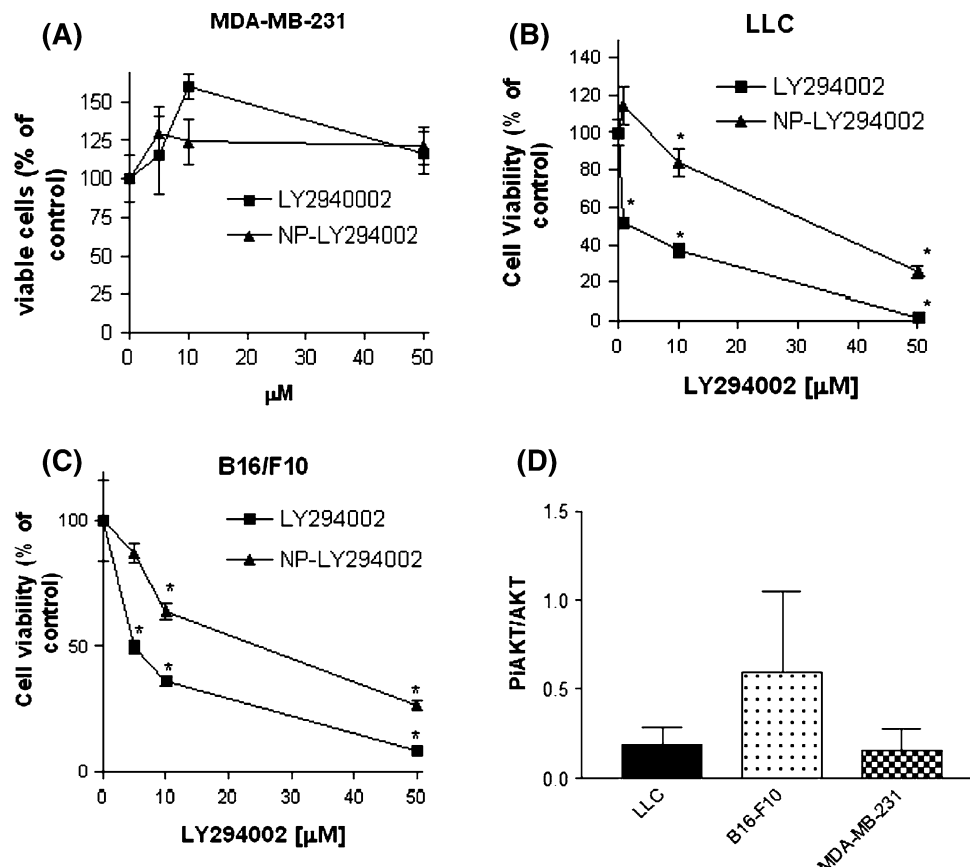
Nanotechnology has made tremendous progress in the recent years and has evolved into a truly interdisciplinary field bridging material science with medicine. The promise of nanotechnology lies in the ability to engineer customizable nanoscale constructs that can be loaded with one or more payloads such as chemotherapeutics, targeting units, imaging and diagnostic agents [19, 20]. In the current study, we engineered LY294002-entrapped nanoparticles (NP-LY) using an emulsion–solvent evaporation technique (Fig. 1a), which resulted in generation of spherical nanoparticles as seen in the transmission electron micrograph with a size range of 110.2 ± 5.9 nm in diameter as confirmed from DLS measurements (Fig. 1b, c, d). It is well documented that nanoparticles in the optimal size range of 80–120 nm preferentially home into tumors by avoiding the reticuloendothelial system [21]. The loading of the encapsulated LY294002 was determined to be 2.98 ± 0.16 μ g per mg of the LY-NP ($n = 7$ independent batches) as determined by UV–VIS spectroscopy at the characteristic wavelength of LY294002 ($\lambda = 298$ nm) (Fig. 1e). Drug release from nanoparticles and subsequent degradation is critical for biologic activity, and depends on desorption of surface-bound drugs, diffusion through the nanoparticle matrix, and erosion of the nanoparticle matrix

[22]. We evaluated the release kinetics of LY294002 from the NPs incubated with cell lysates, which mimics the *in vivo* situation, wherein the tumor interstitial fluid is an acidic and enzyme-enriched leachate formed from the necrotic cells. Consistent with previous reports on nanoparticles with drug loaded in the matrix, there was a rapid release of LY294002 within 7 h of incubation; it then started to decay and became saturated after 10 h, with sustained release for up to 72 h (Fig. 1f). Interestingly, the rate and amount of LY294002 released from the nanoparticles was dependent on the cell type, with maximal release evident when incubated with HUVECs. The release kinetics was similar when incubated with either MDA-MB-231 or B16-F10 cells (Fig. 1f).

To measure cytotoxicity of NP-LY versus the free drug, we incubated a panel of three cancer cell lines with free LY294002 or nanoparticle containing an equivalent amount of LY294002 for 24, 48, and 72 h, following which we measured the metabolic activity of these cells using 3-(4,5-Dimethylthiazol-2-yl)-5-(3-carboxymethoxyphenyl)-2-(4-sulfophenyl)-2H-tetrazolium (MTS). As shown in Fig. 2a–c and supplementary Fig. 1, a slower onset of cytotoxic effect was observed following NP-LY treatment as compared with the free drug (LY294002), thus

confirming the temporal control over the release exerted by encapsulating LY294002 in the nanoparticles. Interestingly, we observed different levels of susceptibility to the NP-LY treatment between the cancer cell lines. Significant cytotoxic effect on MD-MB-231 breast adenocarcinoma cells was apparent only at the higher concentrations and following 72 h of incubation. In contrast, NP-LY significantly inhibited the viability of LLC and B16-F10 cells. For example, following 48 h of incubation with 50 μ M of LY294002 or NP-LY, the proportion of viable cells as percentage of vehicle-treated control were 116% and 122% for MDA-MB-231, 2 and 25% for LLC and 8 and 27% for B16-F10, respectively, suggesting that MDA-MB-231 was refractory while both B16-F10 and LLCs were sensitive to the treatments with LY294002 or NP-LY. For further studies we therefore selected B16/F10 and MDA-MB-231 cell lines as examples of susceptible and refractory cells, respectively. Interestingly, while the mean level of activated Akt (downstream of PI3K) was higher in B16/F10 cells, the difference with the levels in the other cell lines was statistically not significant (Fig. 2d), which indicated that the refractoriness to nanoparticle-mediated targeting could be independent of activation status of the target protein.

Fig. 2 Concentration–effect of NP-LY on viability of cancer cells. **a–c** Graph shows the viability of Breast adenocarcinoma (MDA-MB-231), Lewis lung carcinoma (LLC) and melanoma (B16-F10) cells treated with either free drug (LY) or LY-encapsulated nanoparticles (NP-LY) for 48 h. The viability of cells was quantified using the MTS assay. Data represents mean \pm SEM from independent triplicates. * $P < 0.05$ compared with vehicle-treated control cells (ANOVA). **d** Basal level of activation of PI3K signaling in the three cell lines as quantified by western blotting for phosphorylated Akt. Data expressed is mean \pm SEM ratio of phosphoAkt/total Akt from $n = 3$ independent experiments. The intensity of chemiluminescent signal was quantified using a Syngene image analysis system



To rationalize the differential sensitivity between both cell lines to the treatments, we evaluated the mechanisms of nanoparticle internalization using the LysoTracker Red probe. We engineered nanoparticles from fluorescein-labeled PLGA. B16-F10 or MDA-MB-231 cells were treated with FITC-nanoparticles for defined time periods. Lysosomal compartments of live cells were then stained with LysoTracker Red probe and visualized using epifluorescence microscopy such that the merged images would appear yellow if the green FITC-nanoparticle were internalized into the red-labeled lysosomes. As seen in Fig. 3a, nanoparticles were taken up by the B16-F10 cells earlier as compared with MDA-MB-231, with significant internalization occurring as early as 15 min in B16-F10, whereas comparable internalization was only observed at later time points in MDA-MB-231 cells. Furthermore, the colocalization of the FITC-nanoparticles and the LysoTracker Red signals indicated that the nanoparticles were internalized into the lysosomes. This is a critical observation as this indicates that the acidic pH and the lysosomal enzymes can facilitate the accelerated breakdown of the

PLGA, releasing the entrapped LY294002 from the matrix. The limited/delayed internalization of the nanoparticle into the lysosomes of the MDA-MB-231 cells could therefore explain the refractoriness of the cell line to the treatment. Alternatively, it could be correlated with the over-expression of ATP-binding cassette (ABC) transporters, which have been implicated in conferring refractoriness to drugs in this cell line by actively excreting the drug [23]. The exact mechanism underlying the limited efficacy seen with LY294002 in MDA-MB-231 remains to be investigated.

To further evaluate the underlying mechanisms of action of LY294002-nanoparticles in cancer cells, MDA-MB-231 and B16-F10 were treated with 50 μ M of LY294002 or NP-LY and subjected to immunoblotting for quantifying the levels of phospho- and total AKT. It is now well established that the activation of PI3K results in the generation of PIP3 on the inner leaflet of the plasma membrane, which recruits AKT by direct interaction with its PH domain [24]. At the membrane a serine/threonine kinase, PDK1, phosphorylates AKT on Thr308, which activates AKT. A second phosphorylation at Ser473 increases the

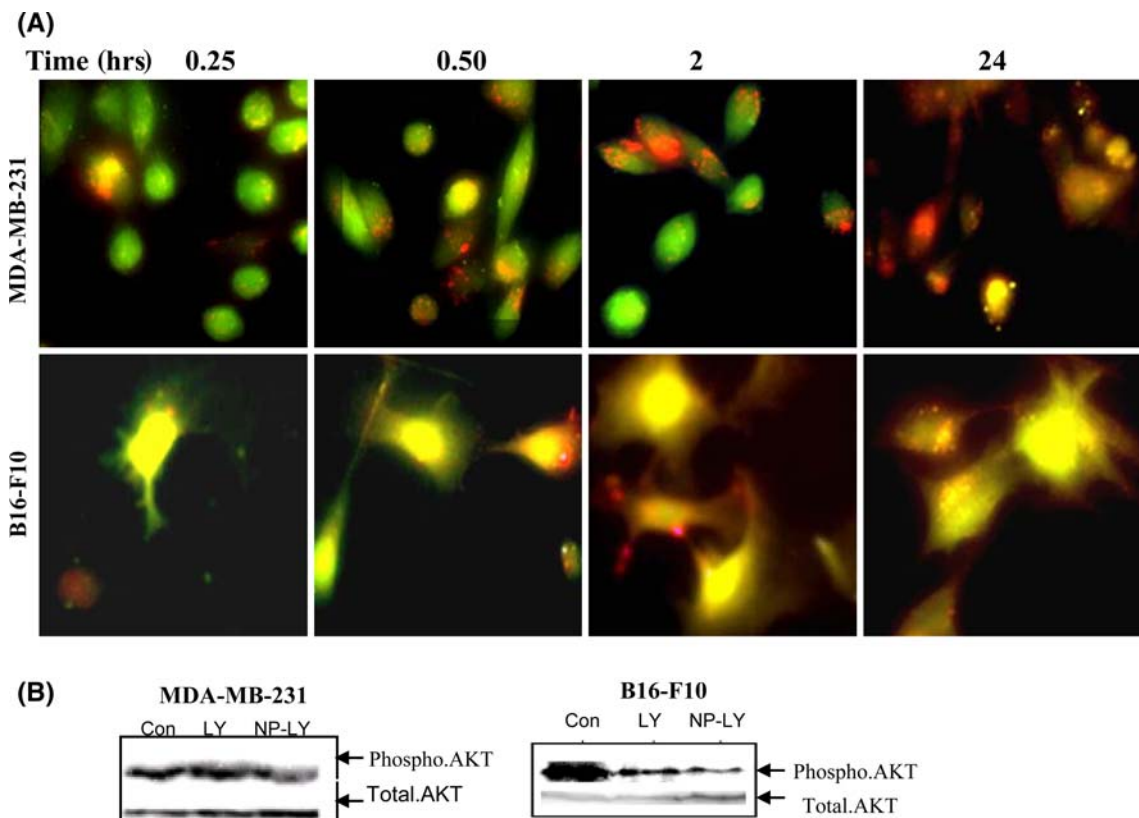


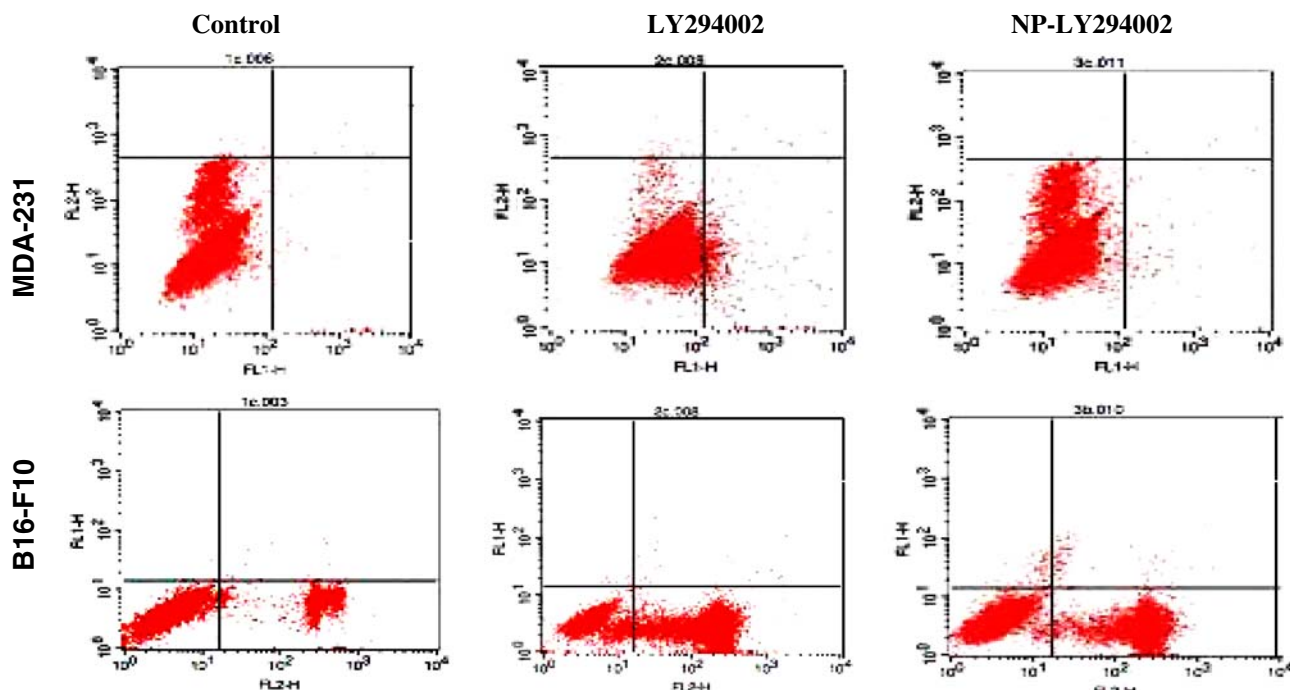
Fig. 3 Mechanisms of nanoparticle uptake and downstream activity in cancer cells. **a** Representative immunofluorescence images show the localization of FITC-labeled nanoparticles. Breast adenocarcinoma (MDA-MB-231) and melanoma cells (B16-F10) were seeded on glass coverslips in 24-well plates and incubated with FITC-labeled nanoparticles. At indicated time points, cells were stained with

LysoTracker Red to label the lysosomes, fixed and subjected to fluorescence microscopy at 40 \times magnification. **b** A representative blot from independent triplicates show the effect of NP-LY and free LY294002 treatments on the levels of phospho-Akt in B16/F10 and MDA-MB-231 cells

activity. Indeed, AKT was found to be phosphorylated in both MDA-MB-231 and B16/F10 melanoma cells. Interestingly, whereas treatment with LY294002 or NP-LY had only minimal effect on inhibiting the phosphorylation of AKT in MDA-MB-231 cells, both free LY294002 and NP-LY inhibited AKT signaling in B16-F10 cells by up to 7-fold (Fig. 3b). Together with the uptake studies, this differential inhibition of AKT signaling could potentially explain the distinct sensitivities of MDA-MB-231 and B16-F10 with respect to both free and encapsulated LY294002.

One of the key biologic consequences of activated AKT signaling is the inhibition of apoptosis through phosphorylation of several components of the cell death machinery. For example, AKT-mediated phosphorylation of BAD, a pro-apoptotic member of the BCL2 family of proteins, prevents its nonfunctional heterodimerization with the

survival factor BCL-X_L, leading to restoration of the antiapoptotic function of BCL-X_L [25]. Furthermore, AKT-induced phosphorylation can inhibit the catalytic activity of pro-apoptotic caspase-9 [26] and also prevent the nuclear translocation of FKHR, a member of the Forkhead family of transcription factors, resulting in inactivation of FKHR gene targets including pro-apoptotic proteins such as BIM and FAS ligands [27]. To determine whether the LY294002 and NP-LY-induced inhibition of PI3K and subsequent block of AKT activation results in apoptosis of tumor cells, we labeled the cells with AnnexinV (conjugated to FITC), which binds to phosphatidylserine expressed on cell surface during apoptosis. Simultaneous staining of the cells with the vital dye, propidium iodide (PI), allowed us to get a profile of early (AnnexinV-FITC +ve, PI-ve) versus late (AnnexinV-FITC +ve;



MDA-MB-231	Control \pm SE	LY294002 \pm SE	NP-LY \pm SE
UL	0.21 \pm .04	0.30 \pm .13	0.15 \pm .06
UR	0.21 \pm .03	0.09 \pm .02	0.05 \pm .01
LL	98.21 \pm .23	96.49 \pm .50	99.23 \pm .09
LR	1.36 \pm .22	3.11 \pm .62	0.57 \pm .09

B16-F10	Control \pm SE	LY294002 \pm SE	NP-LY \pm SE
UL	0.02 \pm .01	0.10 \pm .03	0.39 \pm .12
UR	0.16 \pm .06	0.22 \pm .09	0.47 \pm .17
LL	72.45 \pm .74	38.05 \pm .398	64.09 \pm .61
LR	27.36 \pm .781	61.64 \pm .391	35.04 \pm .47

Fig. 4 Treatment with LY294002 or NP-LY induces apoptosis. The percentages of early and late apoptosis stages were quantified using the Annexin V-FITC/propidium iodide FACS assay. Cells were treated with LY or NP-LY for 48 h and then subjected to FACS analysis. Cells were gated into four quadrants based on red (FL2-H)

versus green (FL1-H) fluorescence. The percentage of cells in each quadrant is shown in the tables below and is expressed as mean \pm SEM. Images shown are representatives from independent triplicates

PI +ve) apoptosis (Fig. 4). Fluorescence activated cell sorting analysis following annexinV-FITC and PI staining revealed that only 3.11 and 0.09% of the MDA-MB-231

cells were in early and late apoptosis following LY294002 treatment. Similarly, treatment with NP-LY resulted in 0.57 and 0.05% of the MDA-MB-231 cells in early and late

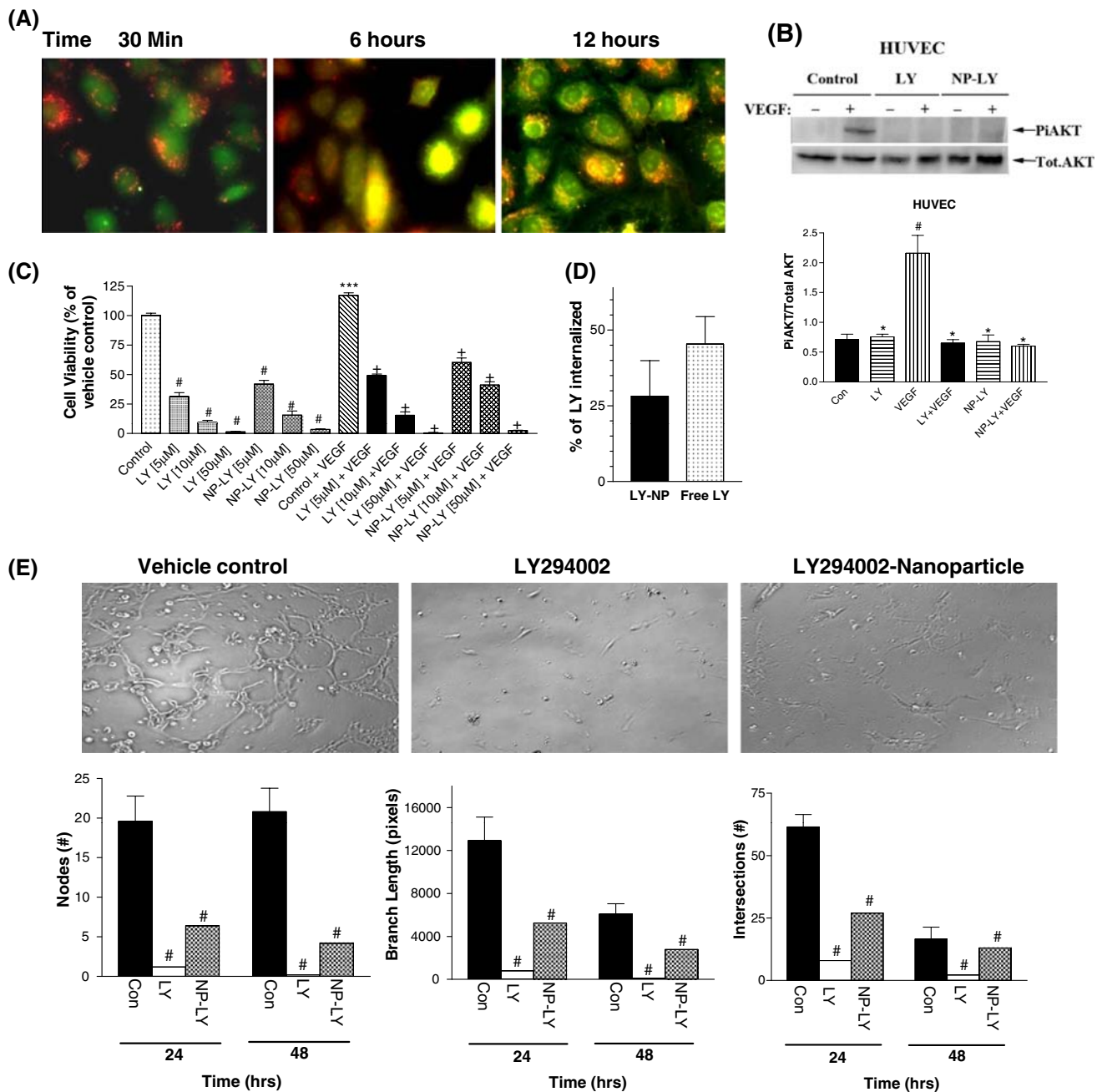


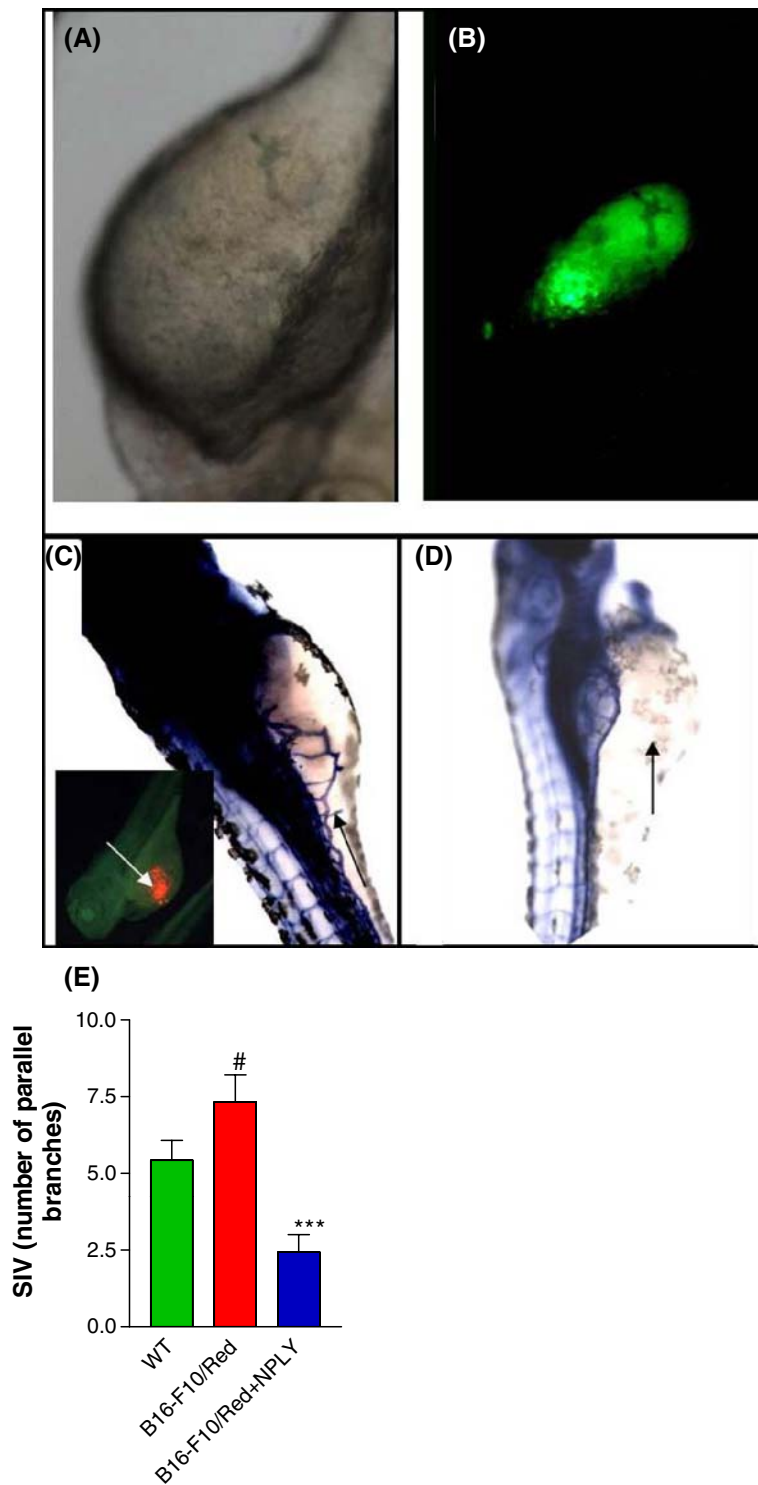
Fig. 5 Effect of NP-LY on angiogenesis in vitro. **a** Immunofluorescence images show the temporal uptake of FITC-labeled nanoparticles in HUVECs, which were counterstained with LysoTracker Red. **b** Representative western blot showing phospho and total Akt levels in HUVEC treated with LY294002 or NP-LY for 24 h, followed by 15 min of VEGF. The graph shows densitometric analysis of intensity levels of the chemiluminescent signal from $n = 2$ independent experiments. **c** Graph shows the effect of different treatments on VEGF-induced proliferation of HUVECs. The viability of the cells was quantified using the MTS assay. Data shows mean \pm SEM ($n = 3$). $^{\#}$ P , *** $P < 0.001$ vs vehicle-treated controls. $+$ $P < 0.05$

vs VEGF-treated group. **d** Graph shows the intracellular levels of LY294002 when the HUVECs were incubated with free LY294002 or nanoparticles loaded with an equivalent concentration of LY294002. Data represents mean \pm SEM from at least independent triplicates. **e** Representative micrographs show the effects of LY294002 and NP-LY on HUVEC tube formation were quantified by seeding cells on matrigel in the presence or absence of the drugs for 24 and 48 h. Graphs show the quantification of the images using three morphometric analyses. Data shows mean \pm SEM. $^{\#}$ $P < 0.05$ vs vehicle-treated controls

apoptosis phases, respectively. In contrast, treatment of B16/F10 melanoma cells with LY294002 resulted in 61.64 and 0.22% of the cells shifting to early and late apoptosis, respectively. Similarly, treatment with NP-LY resulted in 35.04 and 0.47% of the cells shifting to early and late apoptosis, consistent with the temporal nature release of

LY294002 from the nanoparticles. Intriguingly, the failure of LY294002 or NP-LY to induce apoptosis in the MDA-MB-231 cell line despite the basal activated state of AKT in this cell line is not entirely unexpected. While it may arise from reduced uptake or increased efflux of the nanoparticle inside the cells, as observed in this study, it

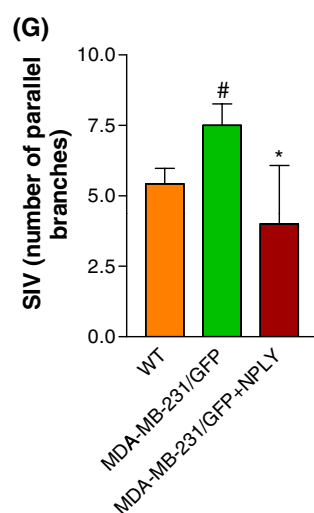
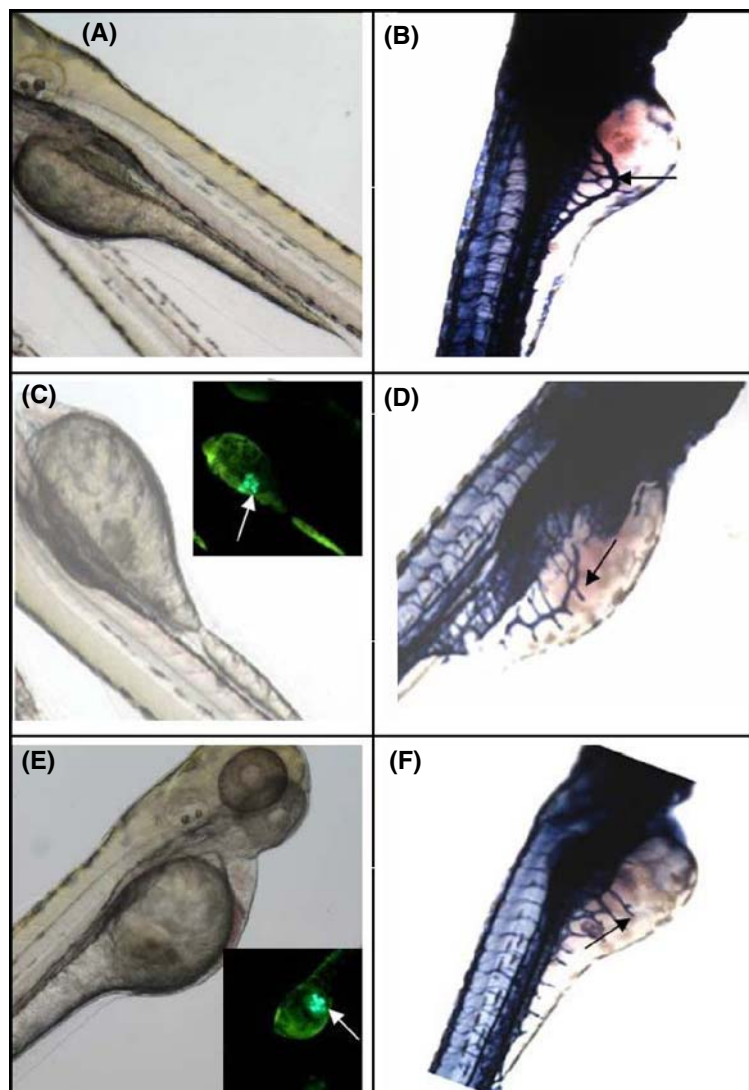
Fig. 6 Effects of NP-LY on B16-F10-mediated angiogenesis *in vivo* using a zebrafish xenograft assay. Zebrafish were xenografted with matrigel-encapsulated B16-F10 melanoma cells labeled with QTracker Red. The cells were injected into the yolk in close proximity to the subintestinal vessels. Zebrafish embryos were injected with FITC-nanoparticle and visualized 2 days post injection (2 dpi) under **a** bright field and **b** fluorescence microscopy, respectively. Treatment with vehicle had no effect on angiogenesis induced by the tumor cells (**c**), while injecting NP-LY completely abrogated the angiogenic response (**d**). The vasculature was stained (blue) using alkaline phosphatase staining and the subintestinal vessels (*black arrows*) were imaged under bright field microscopy. Fish were also imaged under fluorescence in order to visualize the cancer cells, which were localized next to the subintestinal vessels (**c** inset, *white arrow*). **e** Graph shows morphometric quantification of the effect of treatment on xenograft-induced angiogenesis. Data shown are mean \pm SEM ($n = 16$). $^{\#} P < 0.05$ compared with WT embryos. $^{***} P < 0.01$ compared with B16-F10/Red xenografts



may also arise from compensatory mechanisms that are simultaneously activated in cancer cells [28, 29]. For example, in an elegant study, Rosen et al. demonstrated

that induction of PTEN (thereby downregulation of PI3K signaling) and inhibition of epidermal growth factor receptor induced a synergistic apoptosis response [30] by

Fig. 7 Effects of NP-LY on MDA-MB-231/GFP-mediated angiogenesis *in vivo* using the zebrafish xenograft assay. Zebrafishes were transplanted with matrigel-encapsulated GFP-labeled MDA-MB-231 cells, in the absence (**c, d**) or presence (**e, f**) of NP-LY for 2 days, as in Fig. 6. Wild type (uninjected) fish served as internal controls (**a, b**). Representative bright field and fluorescent images taken in real-time are shown in the *left panels*, whereas alkaline phosphatase vessel staining is shown on the *right panels*. **g** Graph represents morphometric quantification of the effect of treatment on xenograft-induced angiogenesis. Data shown are mean SEM ($n = 3–10$). *Black* arrows = subintestinal vessels; *white arrows* = MDA-MB-231/GFP. $\# P < 0.05$ compared with WT embryos. $* P < 0.05$ compared with MDA-MB-231/GFP xenografts (ANOVA followed by Newman Keuls Post test)



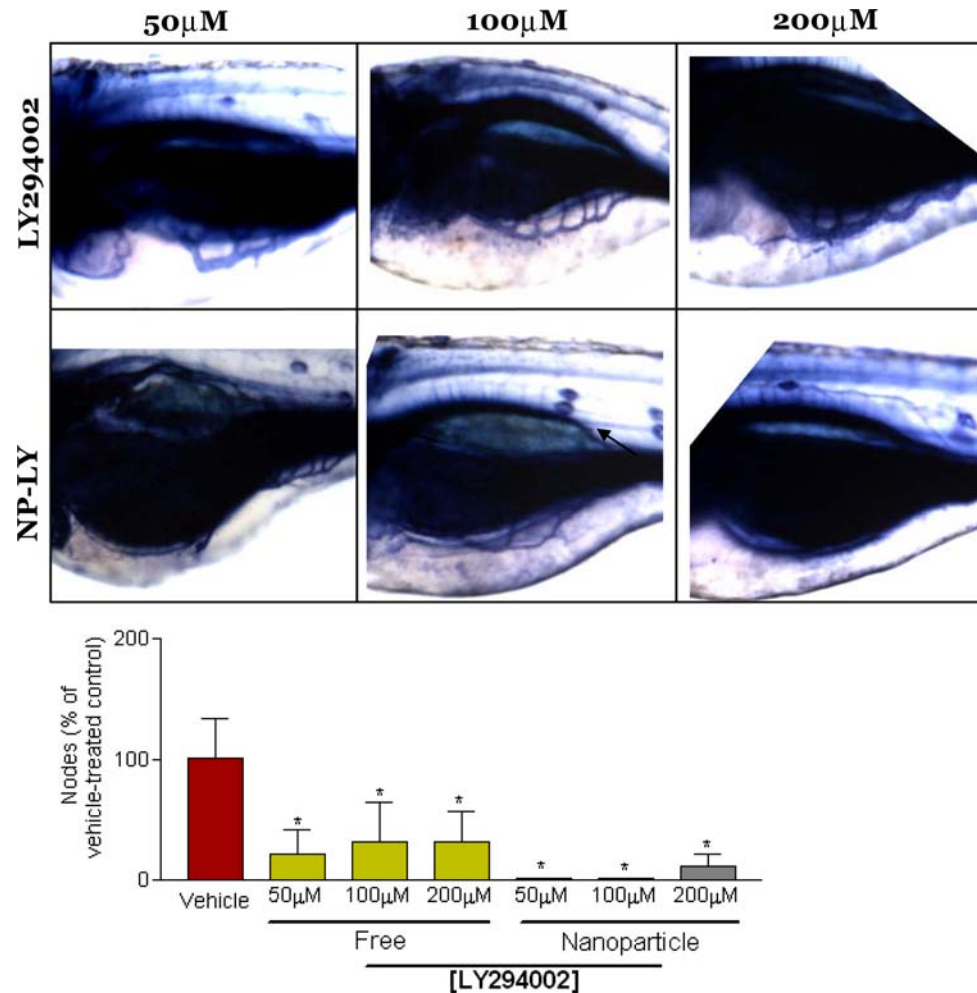
blocking distinct pathways that independently converge into phosphorylation of the pro-apoptotic protein BAD at two distinct sites. Indeed, in another study, a combination of an AKT/mammalian target of rapamycin (mTOR) inhibitor and a MAPK kinase 1 inhibitor were shown to dramatically impact tumor progression in a hormone-refractory prostate cancer model [31], indicating that tumor progression can depend on multiple independent signaling pathways, and any broad nanoparticle-based strategy for targeting tumor cells will potentially require the inhibition of multiple targets besides PI3K.

A key event during tumor progression is the requirement for angiogenesis, or the formation of new blood vessels from an existing vascular bed in order for the tumor to grow beyond 1 mm^3 in volume [32]. This ‘angiogenic switch’ has been implicated as a critical step for tumor progression and metastasis [33]. Interestingly, a critical promoter for tumor angiogenesis is the activation of the PI3K/AKT pathway. We rationalized that the discrepancy in the susceptibility of different tumors to PI3K inhibitors could potentially be overcome by nanoparticle-mediated targeting of the

activated PI3K/AKT signaling cascade in endothelial cells, given that the angiogenic process is consistent across different tumors. Indeed as shown in Fig. 5a, we observed a rapid uptake of the FITC-labeled NP-LY into human umbilical vein endothelial cells (HUVECs) within 30 min of incubation, with internalization into the lysosomes clearly evident by 6 h, as seen from the colocalization of the signals from the FITC-nanoparticle and the Lysotracker Red-labeled lysosomes. Interestingly the FITC signal and the Lysotracker signal disengaged by 12 h, suggesting that the nanoparticles are processed in the lysosomes and the active agents are released into the cytosol. Furthermore, the intracellular level of LY294002 following incubation of the cells with LY-NP or LY294002 was found to be similar (Fig. 5d). Indeed, western blot analysis of the activated Akt revealed that 24 h incubation with both LY294002 and NP-LY at 50 μM concentration resulted in complete inhibition of VEGF-induced activated PI3K-mediated phosphorylation of Akt in the HUVEC cells (Fig. 5b).

The angiogenesis process involves a temporal series of discrete but overlapping steps, including proliferation and

Fig. 8 Dose–effect of free LY294002 or NP-LY on B16-F10-mediated angiogenesis in vivo. Zebrafishes were transplanted with B16/F10 cells along with free drug or NP-LY (50, 100 and 200 μM). After 2 dpi, the vasculature was stained for alkaline phosphatase expression. Representative bright field images show effect of different concentrations of free LY294002, or an equivalent concentration of LY294002 in the nanoparticle on xenograft-induced angiogenesis from the SIV. Graph shows morphometric quantification (mean \pm SEM number nodes in SIV $n = 13\text{--}15$). $^{\#} P < 0.05$ compared with B16-F10/Red xenografts



tubulogenesis of endothelial cells [34]. We decided to evaluate the activity of the NP-LY on endothelial cell proliferation. Serum-starved synchronized HUVECs were stimulated with vascular endothelial growth factor (VEGF) in the presence of increasing concentrations of LY294002 or NP-LY. Cell proliferation at the end of 48 h was quantified using an MTS assay. As shown in Fig. 5c, treatment with LY294002 or LY-nanoparticle blocked VEGF-induced cell proliferation, consistent with the inhibition of PI3K signaling.

During angiogenesis, proliferation of endothelial cells is followed by tubulogenesis, which is mimicked when endothelial cells are plated on growth factor-enriched matrigel, a tumor extracellular matrix. As shown in Fig. 5e, HUVECs formed a well-developed vascular network of tubes on matrigel in the vehicle-treated group, which was inhibited by LY294002 and NP-LY (Fig. 5e). Interestingly, while both free LY294002 and NP-LY significantly inhibited tube formation within 24 h, the free drug was more potent, confirming the temporal nature of release of active drug from the nanoparticle. These results indicated that PI3K plays a key role in critical steps of angiogenesis, and therefore could emerge as an exciting target for the inhibition of tumor angiogenesis, consistent with earlier observations [35].

To test whether the NP-LY can inhibit angiogenesis *in vivo*, we harnessed a zebrafish tumor xenograft model, which has evolved as a powerful model for studying angiogenesis [36]. As shown in Fig. 6a, b, the injected nanoparticles (FITC-labeled) were restricted in close proximity to the subintestinal vessels, and by themselves, did not induce cytotoxicity. Similarly, the Qtracker-labeled B16/F10 cells were found to be viable and growing in the yolk, in close proximity to SIV space (Fig. 6c inset), and in some cases exhibited metastasis (results are not shown). The tumor cells were found to induce angiogenesis as clearly seen from the remodeling or budding of vascular structures from the subintestinal vessels, consistent with previous observations [37]. The presence of NP-LY completely inhibited angiogenesis from the subintestinal vessel (Fig. 6d). Similarly, in fish injected with MDA-MB-231/GFP cells, morphometric analysis revealed that the xenograft-induced angiogenesis was significantly greater than the angiogenesis observed in vehicle-controls (Fig. 7a–d). Interestingly, the injection of NP-LY abrogated this vessel development (Fig. 7e–f). Additionally, in a dose-efficacy study, we observed a marked variability with the free LY294002 as compared with the robust antiangiogenic response elicited by NP-LY, which could arise from the sustained local delivery of LY294002 from the nanoparticles (Fig. 8). Our results suggest that nanoparticle-mediated delivery of PI3K inhibitors for targeting tumor angiogenesis could be an attractive approach, even if there are differences

in the susceptibility of tumor cells to nanoparticle-mediated inhibition of PI3K. While the zebrafish assay is not optimized for doing homing studies, the preferential passive homing to angiogenic vessels by nanoparticle is well documented [38, 39] and, to the best of our knowledge, has not been shown to be taken up by endothelial cells lining normal vessels. However, it is likely that nanoparticles can be internalized by endothelial cells lining angiogenic tumor vasculature, which exhibit abnormal flow dynamics or stasis. Targeting the tumor vasculature can further be optimized by decorating the nanoparticle surface with ‘homing’ peptides against epitopes specifically expressed on tumor vasculature, such as $\alpha v \beta 3$ integrins [40]. Indeed an optimal strategy for effective anticancer outcome could combine such a signal-transduction inhibition-based antiangiogenesis approach with a cytotoxic chemotherapeutic agent for optimal anticancer outcome, which we are currently exploring in our laboratory.

Acknowledgments This work was supported by a Department of Defense BCRP Era of Hope Scholar award [W81XWH-07-1-0482] and Mary Kay Ash Charitable Foundation Grant to SS. DH is supported by an AHA Fellow to Faculty Transition Grant and RH is supported by a CIHR Fellowship. We thank Prof. Joseph Bonventre for access to his laboratory and Nicki Watson, Imaging Facility at Whitehead Institute for Biomedical, for the electron microscopy studies.

References

1. Vivanco I, Sawyers CL (2002) The phosphatidylinositol 3-Kinase AKT pathway in human cancer. *Nat Rev Cancer* 2:489–501
2. Datta SR, Brunet A, Greenberg ME (1999) Cellular survival: a play in three Akts. *Genes Dev* 13:2905–2927
3. Shayesteh L, Lu Y, Kuo WL, Baldocchi R, Godfrey T, Collins C, Pinkel D, Powell B, Mills GB, Gray JW (1999) PIK3CA is implicated as an oncogene in ovarian cancer. *Nat Genet* 21:99–102
4. Engelman JA, Chen L, Tan X, Crosby K, Guimaraes AR, Upadhyay R, Maira M, McNamara K, Perera SA, Song Y, Chiriac LR, Kaur R, Lightbody A, Simendinger J, Li T, Padera RF, García-Echeverría C, Weissleder R, Mahmood U, Cantley LC, Wong KK (2008) Effective use of PI3K and MEK inhibitors to treat mutant Kras G12D and PIK3CA H1047R murine lung cancers. *Nat Med* 14:1351–1356
5. Koul D (2008) PTEN signaling pathways in glioblastoma. *Cancer Biol Ther* 7:1321–1325
6. Petrocelli T, Slingerland JM (2001) PTEN deficiency: a role in mammary carcinogenesis. *Breast Cancer Res* 3:356–360
7. Steelman LS, Stadelman KM, Chappell WH, Horn S, Bäsecke J, Cervello M, Nicoletti F, Libra M, Stivala F, Martelli AM, McCubrey JA (2008) Akt as a therapeutic target in cancer. *Expert Opin Ther Targets* 12:1139–1165
8. Iwanaga K, Yang Y, Raso MG, Ma L, Hanna AE, Thilaganathan N, Moghaddam S, Evans CM, Li H, Cai WW, Sato M, Minna JD, Wu H, Creighton CJ, Demayo FJ, Wistuba II, Kurie JM (2008) Pten inactivation accelerates oncogenic K-ras-initiated tumorigenesis in a mouse model of lung cancer. *Cancer Res* 68:1119–1127
9. Horie Y, Suzuki A, Kataoka E, Sasaki T, Hamada K, Sasaki J, Mizuno K, Hasegawa G, Kishimoto H, Iizuka M, Naito M, Enomoto K, Watanabe S, Mak TW, Nakano T (2004) Hepatocyte-

specific Pten deficiency results in steatohepatitis and hepatocellular carcinomas. *J Clin Invest* 113:1774–1783

10. Yuan TL, Choi HS, Matsui A, Benes C, Lifshits E, Luo J, Frangioni JV, Cantley LC (2008) Class 1A PI3K regulates vessel integrity during development and tumorigenesis. *Proc Natl Acad Sci U S A* 105:9739–9744
11. Sengupta S, Sellers LA, Li RC, Gherardi E, Zhao G, Watson N, Sasisekharan R, Fan TP (2003) Targeting of mitogen-activated protein kinases and phosphatidylinositol 3 kinase inhibits hepatocyte growth factor/scatter factor-induced angiogenesis. *Circulation* 107:2955–2961
12. Sengupta S, Sasisekharan R (2007) Exploiting nanotechnology to target cancer. *Br J Cancer* 96(9):1315–1319
13. Yuan F, Leunig M, Huang SK, Berk DA, Papahadjopoulos D, Jain RK (1994) Microvascular permeability and interstitial penetration of sterically stabilized (stealth) liposomes in a human tumor xenograft. *Cancer Res* 54:3352
14. Ibrahim NK, Desai N, Legha S, Soon-Shiong P, Theriault RL, Rivera E, Esmaeli B, Ring SE, Bedikian A, Hortobagyi GN, Ellerhorst JA (2002) Phase I and pharmacokinetic study of ABI-007, a Cremophor-free, protein-stabilized, nanoparticle formulation of paclitaxel. *Clin Cancer Res* 8:1038–1044
15. Stavridi F, Palmieri C (2008) Efficacy and toxicity of nonpegylated liposomal doxorubicin in breast cancer. *Expert Rev Anticancer Ther* 8:1859–1869
16. Basu S, Harfouche R, Soni S, Chimote G, Mashelkar RA, Sengupta S (2009) Nanoparticle-mediated targeting of MAPK signaling predisposes tumor to chemotherapy. *Proc Natl Acad Sci U S A* 106(19):7957–7961
17. Vlahos CJ, Matter WF, Hui KY, Brown RF (1994) A specific inhibitor of phosphatidylinositol 3-kinase, 2-(4-morpholinyl)-8-phenyl-4H-1-benzopyran-4-one (LY294002). *J Biol Chem* 269:5241–5248
18. Nicoli S, Presta M (2007) The zebrafish/tumor xenograft angiogenesis assay. *Nat Protoc* 2:2918–2923
19. Ferrari M (2005) Cancer nanotechnology: opportunities and challenges. *Nature Rev Cancer* 5:161–171
20. Peer D, Karp JM, Hong S, Farokhzad OC, Margalit R, Langer R (2007) Nanocarriers as an emerging platform for cancer therapy. *Nature Nanotech* 2:751–760
21. Moghimi SM, Hunter AC, Murray JC (2005) Nanomedicine: current status and future prospects. *FASEB J* 19(3):311–330
22. Soppimath KS, Aminabhavi T, Kulkarni AR, Rudzinski WE (2001) Biodegradable polymeric nanoparticles as drug delivery devices. *J Controlled Release* 70:1–260
23. Honorat M, Mesnier A, Di Pietro A, Lin V, Cohen P, Dumontet C, Payen L (2008) Dexamethasone down-regulates ABCG2 expression levels in breast cancer cells. *Biochem Biophys Res Commun* 375:308–314
24. Stokoe D, Stephens LR, Copeland T, Gaffney PR, Reese CB, Painter GF, Holmes AB, McCormick F, Hawkins PT (1997) Dual role of phosphatidylinositol-3, 4, 5-trisphosphate in the activation of protein kinase B. *Science* 277:567–570
25. Datta SR, Dudek H, Tao X, Masters S, Fu H, Gotoh Y, Greenberg ME (1997) Akt phosphorylation of BAD couples survival signals to the cell-intrinsic death machinery. *Cell* 91:231–241
26. Cardone MH, Roy N, Stennicke HR, Salvesen GS, Franke TF, Stanbridge E, Frisch S, Reed JC (1998) Regulation of cell death protease caspase-9 by phosphorylation. *Science* 282:1318–1321
27. Brunet A, Bonni A, Zigmond MJ, Lin MZ, Juo P, Hu LS, Anderson MJ, Arden KC, Blenis J, Greenberg ME (1999) Akt promotes cell survival by phosphorylating and inhibiting a Forkhead transcription factor. *Cell* 96:857–868
28. Buck E, Eyzaguirre A, Rosenfeld-Franklin M, Thomson S, Mulvihill M, Barr S, Brown E, O'Connor M, Yao Y, Pachter J, Miglarese M, Epstein D, Iwata KK, Haley JD, Gibson NW, Ji QS (2008) Feedback mechanisms promote cooperativity for small molecule inhibitors of epidermal and insulin-like growth factor receptors. *Cancer Res* 68:8322–8332
29. Grant S (2008) Cotargeting survival signaling pathways in cancer. *J Clin Invest* 118:3003–3006
30. She QB, Solit DB, Ye Q, O'Reilly KE, Lobo J, Rosen N (2005) Nanocarriers as an emerging platform for cancer therapy. *Cancer Cell* 8:287–299
31. Kinkade CW, Castillo-Martin M, Puzio-Kuter A, Yan J, Foster TH, Gao H, Sun Y, Ouyang X, Gerald WL, Cordon-Cardo C, Abate-Shen C (2008) Targeting AKT/mTOR and ERK MAPK signaling inhibits hormone-refractory prostate cancer in a pre-clinical mouse model. *J Clin Invest* 118:3051–3064
32. Folkman J (2007) Angiogenesis: an organizing principle for drug discovery? *Nat Rev Drug Discov* 6:273–286
33. Folkman J (2002) Role of angiogenesis in tumor growth and metastasis. *Semin Oncol* 29:15–18
34. Gasparini G, Longo R, Toi M, Ferrara N (2005) Nanocarriers as an emerging platform for cancer therapy. *Nat Clin Pract Oncol* 2:562–577
35. Sengupta S, Sellers LA, Cindrova T, Skepper J, Gherardi E, Sasisekharan R, Fan TP (2003) Cyclooxygenase-2-selective nonsteroidal anti-inflammatory drugs inhibit hepatocyte growth factor/scatter factor-induced angiogenesis. *Cancer Res* 63:8351–8359
36. Schnell CR, Stauffer F, Allegrini PR, O'Reilly T, McSheehy PM, Dartois C, Stumm M, Cozens R, Littlewood-Evans A, García-Echeverría C, Maira SM (2008) Effects of the dual phosphatidylinositol 3-kinase/mammalian target of rapamycin inhibitor NVP-BEZ235 on the tumor vasculature: implications for clinical imaging. *Cancer Res* 68:6598–6607
37. Stoletoev K, Montel V, Lester RD, Gonias SL, Klemke R (2007) High-resolution imaging of the dynamic tumor cell vascular interface in transparent zebrafish. *Proc Natl Acad Sci U S A* 104:17406–17411
38. Sengupta S, Eavarone D, Capila I, Zhao G, Watson N, Kiziltepe T, Sasisekharan R (2005) Temporal targeting of tumour cells and neovasculature with a nanoscale delivery system. *Nature* 436:568–572
39. Kaul G, Amiji M (2004) Biodistribution and targeting potential of poly(ethylene glycol)-modified gelatin nanoparticles in subcutaneous murine tumor model. *J Drug Target* 12:585–591
40. Hood JD, Bednarski M, Frausto R, Guccione S, Reisfeld RA, Xiang R, Cheren DA (2002) Tumor regression by targeted gene delivery to the neovasculature. *Science* 296:2404